appliedoptics

Calibration verification of an underwater hyperspectral imaging push broom instrument to measure light in absolute units and field demonstration

BERNHARD SCHARTMÜLLER,[1,*] ![ORCID] **DAVID MCKEE,**[1,2] ![ORCID] **JØRGEN BERGE,**[1] AND **GEIR JOHNSEN**[3,4] ![ORCID]

[1]*Department of Arctic and Marine Biology, Faculty of Biosciences, Fisheries and Economics, UiT The Arctic University of Norway, NO-9037, Tromsø, Norway*
[2]*Physics Department, University of Strathclyde, Glasgow, Scotland, UK*
[3]*Department of Biology, Norwegian University of Science and Technology (NTNU), Trondheim Biological Station, NO-7491 Trondheim, Norway*
[4]*The University Centre in Svalbard (UNIS), P.O. Box 156, NO-9171 Longyearbyen, Norway*
*bernhard.schartmueller@uit.no

The push broom design of an underwater hyperspectral imaging (UHI) instrument makes it possible to measure angle-resolved spectral radiance $L(\lambda)$ in a plane. We describe the characterization of a commercial UHI instrument (UHI-4, Ecotone AS, Norway) and the spectral, geometric, and radiometric calibration transfer for measuring $L(\lambda)$ in absolute units [$\mu W\, cm^{-2}\, nm^{-1}\, sr^{-1}$]. We present a low-cost instrument characterization approach that is intended to be easily replicated for other users to perform their own calibration transfer. Cross-calibration with a RAMSES-ARC spectroradiometer (TriOS, Germany) in air and in water shows good linear correlation across the observed spectral range and over four orders of magnitude in dynamic range, with the UHI instrument providing higher sensitivity overall.

1. INTRODUCTION

A. Background

Light is electromagnetic (radiant) energy [1] and a main driver of photosynthesis and primary production, which is the foundation of all ecosystems [2]. At the same time, light also influences animal behaviors, both as a zeitgeber [3], through biochemical processes, and as a means of communicating [4], to mention a few. Light is considered as the proximate regulatory signal for diel vertical migration of zooplankton, the largest synchronized animal migration with regard to biomass on earth [5]. To understand how biological systems are working it is therefore essential to collect information about the light climate (intensity, spectrum, and duration of light for a specific location [6]) in which organisms are operating.

The science of measuring electromagnetic energy is called radiometry [7]. There are a variety of radiometric parameters that can be measured, with different applications having specific requirements. For remote sensing ground validation, as well as for marine biology, radiance and various irradiances are the radiometric quantities of interest [8]. See Figs. 1(a)–1(c) for the schematic instrument designs and their respective fields of view

(FOVs). However, these instruments only provide single point measurements. This poses a challenge in a highly heterogeneous light environment, e.g., under sea ice with varying snow depth, ridges, and patches of algae growing on the underside of the ice. To map the spatial variability of the light field and/or algae biomass, instruments must be moved in space under the ice [10]. An imaging instrument with a larger FOV, like the UHI that is scanning in a line, offers an improvement in our capability to map to a light field at a high resolution in space and time. However, because of the unusual optics of the UHI we find it necessary to introduce first the radiometric quantities of interest and compare the traditional instrument designs to the UHI.

B. Radiometric Quantities and Corresponding Instrument Designs

The fundamental radiometric quantity is *(spectral) radiance L* [Fig. 1(c)] [7]. It is defined as the radiant energy ΔQ entering the instrument located at a point $\vec{x}$ during a time interval Δt, centered at the time t as seen in [7]
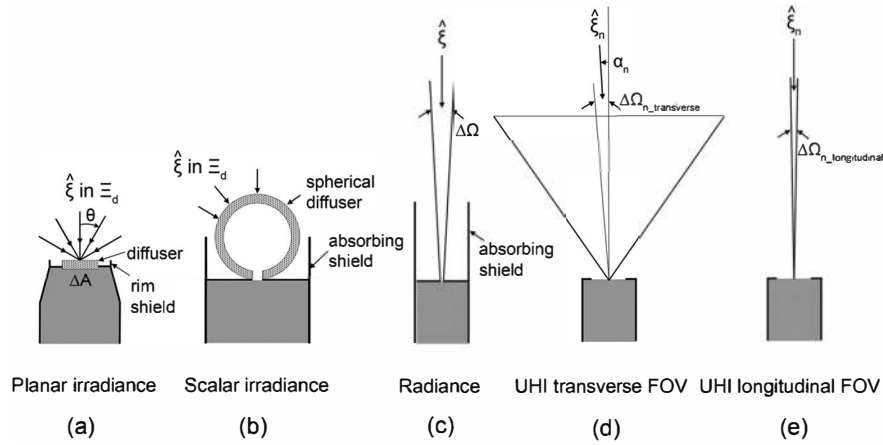
Fig. 1. Schematic design of instruments for measuring light in different radiometric quantities and their respective FOVs. (a) Planar irradiance instrument for measuring photons $\hat{\xi}$ in an entire hemisphere Ξ_d (180°) [7]. (b) Scalar irradiance instrument with spherical diffuser for measuring photons $\hat{\xi}$ in an entire hemisphere Ξ_d (180°) [7]. (c) Radiance instrument measuring photons in a set of directions of solid angle $\Delta\Omega$, centered on direction [7]. (d), (e) FOV of the UHI. Each spatial pixel n collects photons in the transverse FOV $\Delta\Omega_{n\_transverse}$ and longitudinal FOV $\Delta\Omega_{n\_longitudinal}$, centered on the direction $\hat{\xi}_n$. Figure parts (a)–(c) and their captions are adapted from [9].

$$L\left(\vec{x}, t, \hat{\xi}, \lambda\right) \equiv \frac{\Delta Q}{\Delta t \Delta A \Delta \Omega \Delta \lambda} \left[J s^{-1} m^{-2} s r^{-1} nm^{-1}\right]. \tag{1}$$

ΔA represents the detector surface and $\Delta\lambda$ the bandwidth centered at wavelength λ [9]. The instrument collects light traveling in a set of directions of solid angle $\Delta\Omega$ (solid angle is an extension of two-dimensional angle measurements) centered on direction $\hat{\xi}$ [7]. A radiance spectroradiometer has a FOV of several degrees ranging from 1.2° for the SeaPRISM (Cimel Electronique, France) to 7° for the RAMSES-ARC (TriOS Mess- und Datentechnik GmbH, Germany) in air [11]. Radiance specifies the spatial ($\vec{x}$), temporal (t), directional ($\hat{\xi}$), and wavelength (λ) properties of the light field [9]. This makes it possible to derive all other radiometric quantities [9]. However, for certain applications (e.g., the measurement of the photosynthetic rate in aquatic ecosystems [12]) various irradiances might be more relevant and easier to measure [9].

A planar irradiance instrument measures light from a hemisphere (180°) [9] [Fig. 1(a)]. If the instrument is pointed "straight up", it measures light heading downwards (all $\hat{\xi}$ in Ξ_d), which is the spectral downwelling planar irradiance E_d as seen in [9]

$$E_d\left(\vec{x}, t, \lambda\right) \equiv \frac{\Delta Q}{\Delta t \Delta A \Delta \lambda} \left[W m^{-2} nm^{-1}\right]. \tag{2}$$

This assumes that each point of the collector/diffuser is equally sensitive to photons reaching the surface from any angle [7], while the collector/diffuser as a whole is not equally sensitive to all photons headed in downward directions, but produces detector responses proportional to the cosines of the incident photon directions [7]. A planar irradiance instrument effectively integrates the spectral radiance over all downwards directions at 180°, the contribution of each photon weighted by the cosine of the photon's incident angle θ [7]. The relation of the two quantities can be mathematically described as seen in [7]

$$E_d\left(\vec{x}, t, \lambda\right) = \int_{\hat{\xi} \epsilon \Xi_d} L\left(\vec{x}, t, \hat{\xi}, \lambda\right) |\cos\theta| \, d\Omega\left(\xi\right). \tag{3}$$

To design an instrument that is equally sensitive to photons arriving from any direction (360°), the shape of the collector/diffuser has to be changed from flat to spherical [7]. The resulting instrument measures scalar irradiance. If the instrument is equipped with a shield, which is assumed to be completely absorbing and it is pointed straight up only measuring downwards headed photons, it measures the spectral downward scalar irradiance E_{od}, which again can be related to spectral radiance as seen in [7]

$$E_{od}\left(\vec{x}, t, \lambda\right) = \int_{\hat{\xi} \epsilon \Xi_d} L\left(\vec{x}, t, \hat{\xi}, \lambda\right) d\Omega\left(\xi\right). \tag{4}$$

If the orientation of the instrument is reversed, it measures the spectral upward scalar irradiance E_{ou} [7]. If the absorbing shield is removed, photons from all directions are collected (360°) [7]. The resulting quantity is the spectral total scalar irradiance E_o, which is the sum of E_{od} and E_{ou} and can be related to the spectral radiance as seen in [7]

$$E_o\left(\vec{x}, t, \lambda\right) = \int_{\hat{\xi} \epsilon \Xi} L\left(\vec{x}, t, \hat{\xi}, \lambda\right) d\Omega\left(\xi\right). \tag{5}$$

The design of a hyperspectral push broom scanner, such as the UHI, differs considerably from the designs mentioned above. While radiance instruments and irradiance instruments have a radially symmetric FOV, the FOV of a hyperspectral push broom scanner is asymmetric [Figs. 1(d) and 1(e)]. As it scans in a line it has a relatively large FOV in the transverse direction ($\Omega_{transverse}$) and a very narrow FOV in the longitudinal direction ($\Omega_{longitudinal}$). The line is divided in a finite number of spatial pixels. Each spatial pixel has a longitudinal FOV ($\Omega_{n\_longitudinal}$) and a transverse FOV ($\Omega_{n\_transverse}$), with each pixel effectively acting as a spectral radiance sensor. Since each of the spatial pixels is measuring a specific portion of the total FOV, it is possible to measure the angle-resolved radiance.

C. Need for a Low-Cost Calibration Transfer Approach

For ensuring comparability with traditional instruments for measuring radiance a characterization and calibration of the instrument is required. Commercial optical instruments like the UHI usually come with a factory calibration. However, the information about calibration routines provided by the manufacturer can be limited. There is also a risk that the factory calibration is not suitable for a particular application. Therefore, independent cross-checks are recommended [13]. The level of calibration accuracy required is to some extent application-dependent, e.g., remote sensing has a higher requirement to accuracy compared to polar (marine) biology that is dealing with eight to nine orders of magnitude in irradiance [14]. Naturally there is a desire to calibrate with the full range of calibration devices and standards to the best accuracy. However, access to labs equipped for full radiometric calibration to national standards levels is often not possible for a variety of reasons, including cost. The same is true for returning instruments to a manufacturer for recalibration. To sum up, the lack of resources can pose a major obstacle for conducting a calibration. This calls for the development of a low-cost calibration transfer approach that uses equipment that is accessible at most institutions.

There is also the danger of minor damage during transit to and from a manufacturer or during transport and handling in cold climates, e.g., on a snowmobile where vibrations along with low temperatures could damage the optics and electronics. This could limit the value of a remote calibration. There are certainly good grounds for developing the capacity to be able to monitor calibration and independently verify key sensor attributes as they may change over the working lifetime of a sensor.

2. INSTRUMENTATION

This experiment was conducted using two types of hyperspectral sensors, the UHI-4 (Ecotone AS, Norway), which is a hyperspectral imager, and the RAMSES-ARC, a spectroradiometer, whose technical specifications are described in this section.

A. Technical Description of the UHI-4

The UHI-4 (serial number 002) consists of an ORCA-spark digital complementary metal–oxide–semiconductor (CMOS) sensor, a SPECIM V8E spectrograph (80 µm slit width), an 8 mm Cinegon 1.4/8-0902 fore lens [15]. A housing made of titanium GR 5 and a front port of fused silica ensure a depth rating of 3000 m [15] [Fig. 2(a)]. While the spectral range of the CMOS camera is ~300 to ~1000 nm [Fig. 2(b)], within the UHI-4 setup it is limited from 380 to 750 nm [15]. This spectral range is covered by 860 spectral pixels, resulting in a pixel dispersion ranging from 0.4128 nm at ~380 nm to 0.4497 nm at ~750 nm. The radiometric resolution of the UHI-4 is 12-bit (dynamic range) [15] and the spectral resolution of the spectrograph is ~6 nm [19]. The UHI-4 acts as a push broom scanner, which scans in a line with 1920 spatial pixels in a transverse field of view (FOV) covering ~50° (± 25°) in water and ~70° (± 35°) in air. The longitudinal FOV is ~0.4° [15]. See Fig. 2(c) for the optical arrangement and its working principle

(a)

(b)

(c)
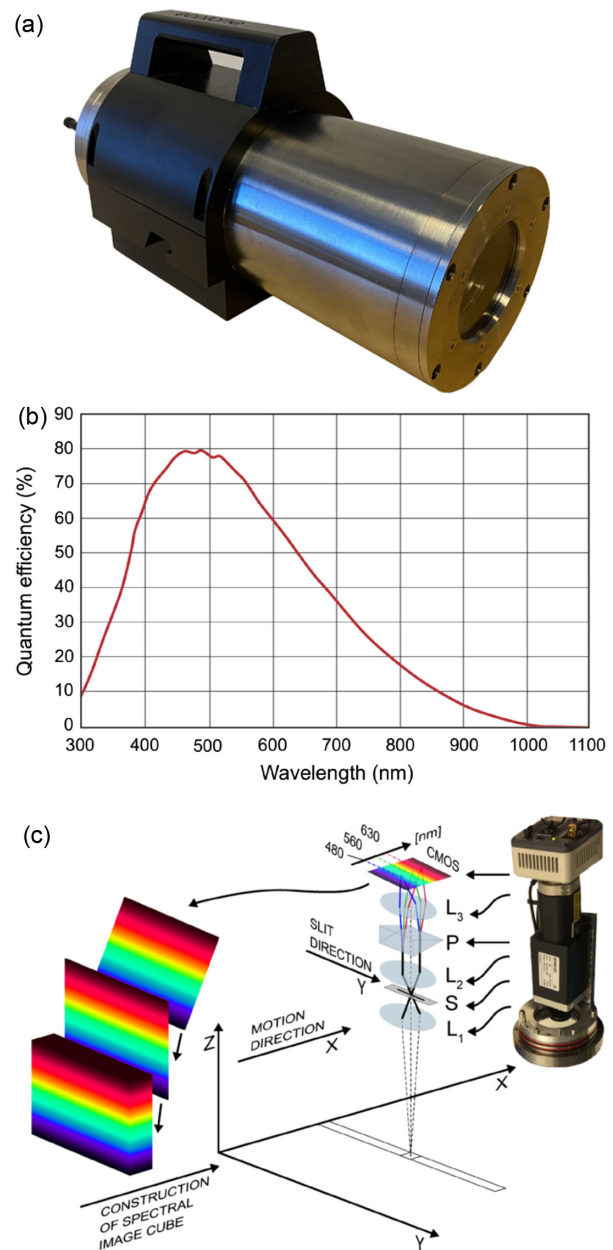
Fig. 2. (a) Picture of the UHI-4 in the 3000 m depth rated underwater housing version. (b) Spectral quantum efficiency response of the CMOS sensor used in the UHI-4. Reprinted from [16] with permission from Hamamatsu Photonics Norden AB. (c) Working principle of a hyperspectral push broom scanner as the UHI-4 and typical optical arrangement. The picture depicts the UHI-4 used in this study taken out of its underwater housing. L_1 = front lens, S = entrance slit, L_2 = collector lens, P = grating prism, L3 = camera lens, CMOS = imaging detector with 1200 spectral pixels and 1920 spatial pixels. Figure (c) redrawn and adapted from [17], with permission of SPIE–the international society for optics and photonics. Representation of hyperspectral data cube was created in a MATLAB script with input from [18].

for deployment. The illustration shows how a spectral image cube is created in a line-to-line approach.

The UHI-4 comprises an imaging system, which is controlled by an on-board computer [15]. This setup allows for two modes of operation, remotely operated and autonomous. For this paper
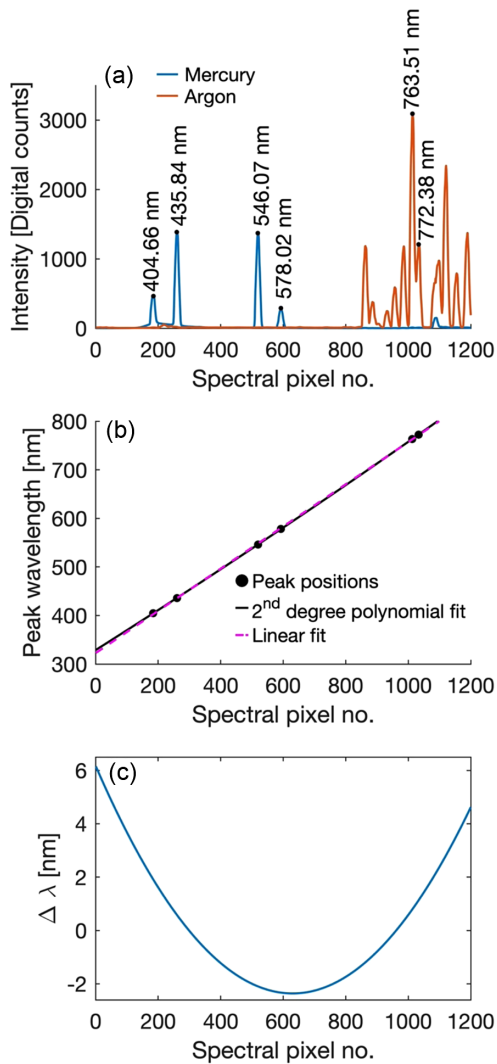
Fig. 3.   (a) Spectra measured of a mercury and an argon lamp for the UHI-4 spatial center pixel. The peaks used for spectral calibration are marked and labeled with the reference wavelengths [24]. (b) Peak wavelengths and corresponding spectral pixel numbers for the UHI-4 spatial center pixel from (a). The magenta line represents a linear fit and the black line a best fit second degree polynomial. When comparing them we see a close to linear relationship. (c) Difference in wavelength between the linear fit and the second degree polynomial fit. The results of the two models are up to ~6 nm, which is a substantial difference.

we operated the UHI-4 remotely via an umbilical connection using "Immersion" acquisition software provided by the manufacturer. The software provides a live stream of hyperspectral data and regular video from an additional camera inside the underwater housing and allows the user to set exposure time (in the interval 1 ms to 10 s), spatial and spectral binning, and gain. The UHI-4 instrument used in this study is equipped with an on-board inertial measurement unit (IMU) that provides navigation data like heading, pitch, roll, acceleration, and magnetic field. A temperature sensor from the CPU of the on-board computer gives an indication for the temperature inside the housing.

B. Technical Description of the RAMSES-ARC Spectroradiometer

RAMSES radiometers (TriOS Mess- und Datentechnik GmbH, Germany) are widely used in the ocean optics community for *in situ* hyperspectral light field measurements ($L(\lambda)$) and spectral irradiances $E(\lambda)$). While the UHI-4 is a line scanner that measures the angular distribution of $L(\lambda)$, the RAMSES-ARC spectroradiometer provides a "point" measurement of $L(\lambda)$ in a FOV of ~7° in air [20]. It operates from 320 to 950 nm with 190 spectral bands (usable channels) [20] giving a lower spectral resolution than the UHI-4, but a greater spectral range. TriOS provides a NIST-traceable radiometric calibration for their RAMSES sensors, which makes them suitable for the radiometric transfer calibration of the UHI-4. However, it is essential that differences in the FOV and spectral resolution are properly accounted for.

3. RESULTS AND DISCUSSION

The unusual optical geometry of the UHI-4 requires development of appropriate calibration approaches [21]. This includes a spectral calibration for assigning a wavelength to each spectral pixel, a geometric calibration for determining the view angle, which is the angle between the principal axis and the light ray that intercepts a particular pixel, of each spatial pixel, and a radiometric calibration that establishes a relationship between the sensor's measurement in digital counts to radiance in [$\mu W\,cm^{-2}\,nm^{-1}\,sr^{-1}$]. Dark current measurements are a prerequisite for the radiometric calibration. We have developed a series of calibration (transfer) techniques to address these issues based on a minimalist approach that is intended to be maximally accessible to labs, and the resulting calibrated data has been tested under field conditions in both air and water.

A. Spectral Calibration

The UHI-4 instrument was spectrally calibrated using two pencil style calibration lamps from Oriel instruments (MKS Instruments, Inc., USA). The argon lamp, a 6030 model, produces spectral lines from argon gas [22], while the mercury lamp, a 6035 Hg (Ar) model, produces spectral lines from the excitation of argon gas and mercury vapor [23]. Both lamps provide a number of well characterized spectral peaks across the visible spectrum. The exact wavelengths used were 404.66, 435.84, 546.07, 576.96, and 579.07 nm for the mercury lamp and 763.51 and 772.38 nm for the argon lamp [24]. However, since the spectral resolution of the spectrograph in the UHI-4 is ~6 nm [25], the mercury peaks at 576.96 and 579.07 nm appear as one "merged" peak in the UHI-4 measurements. Hence, we calculated the mid-point wavelength between these two peaks, 578.02 nm (rounded), for spectral calibration.

Figure 3(a) shows the spectra measured by the spatial center (middle) pixel of the UHI-4 for both lamps. Observed peaks were not symmetrical, so the experimental central pixel was determined as the mid-point of the full-width at half-maximum (FWHM) line rather than the peak position. In the case of the second argon peak at 772.38 nm, 2/3 of the max is used instead of the FWHM because a shoulder of the previous peak would otherwise have influenced the results. The

experimentally derived central spectral pixel numbers (for the spatial center pixel) together with the reference wavelengths were then used to fit a model. We compared a linear model ($p(x) = 0.4345\,x + 322.5764$) and a second degree polynomial model ($p(x) = 2.1499e^{-05}\,x^2 + 0.4074x + 328.7542$). The results in Fig. 3(b) show that there is a primary linear relationship between the spectral pixel numbers and the peak wavelengths. The difference between the two models seems small. This can be explained by the very small number of the quadratic coefficient for the second degree polynomial. However, from calculating the difference in wavelength between the two models [Fig. 3(c)] we can see that the choice of model results in a wavelength difference of up to ~6 nm. This is a substantial difference. Furthermore, we looked at the goodness of fit statistics for both models. For the linear model we get a SSE of 16.0292, an R-square of 0.9999, and a RMSE of 2.0018. For the second degree polynomial model, we get a SSE of 0.2843, an R-square of one, and a RMSE of 0.3078, which is a better fit than the linear model. Thus, the second degree polynomial was then used as the spectral calibration.

B. Geometric Calibration

The goal of the geometric calibration was to identify the view angle for each spatial pixel of the UHI-4. Since the UHI-4 has 1920 spatial pixels along the image slit, it would have been impractical to manually check the view angle of each pixel separately. Instead, we used an approach that uses a target plate consisting of alternating black and white stripes of 750 mm width, which enables identification of the UHI-4 pixel number for each of the transition points. This allowed formulation of a relationship between angle and pixel no. that can then be applied to the entire spatial pixel range.

The UHI-4 was positioned in a perpendicular line towards the center of the target [Fig. 4(a)]. To identify the transition points from black to white fields and vice versa as consistently as possible, it is advantageous that the target plate is illuminated with approximately the same light intensity across its length. This was achieved using a homemade light source that incorporates 3×3 YUJILEDS Full Spectrum CRI 98 COB LED-135L–5600K LEDs mounted on a cooling element. See Fig. 5(b) for the light source and Fig. 5(c) for its spectrum.

The resulting measurements for the geometric calibration (spectral pixel no. 600, approximately 635 nm wavelength) are shown in Fig. 4(b) Note that the optical layout of the UHI-4 is not exactly symmetrical. In Fig. 4(b) black fields can be clearly identified by their low light intensities. The same is valid for white fields that can be identified by their high light intensities. The result is an alternating pattern of high and low light intensities. In addition, the orange tape stripe that was used to mark the center point of the target plate stands out with the overall maximum value. The center point was also used as a reference for measuring the dimensions of the setup and the distances of the black/white transition points. Since the FOVs of neighboring pixels are slightly overlapping the border between black and white fields is more like a short transition range than an abrupt change between a maximum and a minimum. It was therefore decided to use the spatial pixel number that is roughly in the middle between a white field and a black field.
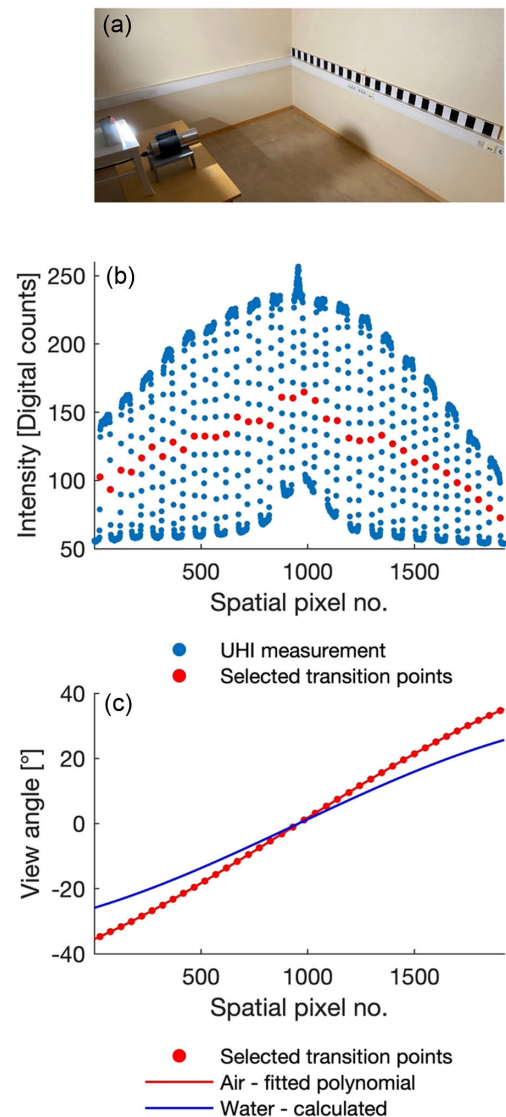
Fig. 4. (a) Setup for geometric calibration with light source placed behind the UHI-4 at a higher level and the UHI-4 pointing at a target plate with alternating black and white stripes. (b) Raw data of measured target plate. The manually selected transition points between black and white stripes are marked in red. (c) Spatial pixel no. for selected transition points and corresponding view angles calculated from distance measurements of the setup. A polynomial fitted through the transition points provides the geometric calibration in air. The in-water view angles are calculated using Snell's law.

Based on the data pairs of spatial pixel number and corresponding dimension that were measured with a folding ruler and a laser distance meter we fitted a curve [Fig. 4(c)]. The best fit was achieved by the following third degree polynomial: ($p(x) = -4.45404704651428e^{-09} x^3 + 1.25111859808384e^{-05} x^2 + 0.0292118794195223 x - 35.4949072424911$, SSE 0.017577, R-square 1, RMSE 0.022737). This polynomial was then used to calculate a view angle for each spatial pixel of the UHI-4. Note, however, that these view angles are only valid in air, but the UHI-4 is also designed to be operated in water. It is therefore necessary to account for the change in view angle caused by the refractive

index of water for in-water deployments. This can be simply solved mathematically by applying Snell's law. We used a refractive index of one for air and 1.33 for water. Note that the refractive index is dependent on wavelength, temperature, pressure, density, and the constituents of water, e.g., salinity [26]. Dependent on the required accuracy this must be considered in the calculations. The calculated view angles for water are shown by the blue line in Fig. 4(c). Note that this reduces the overall FOV from around ~70° in air to ~50° in water.

C. Dark Signal Characterization

Photoelectric devices produce a current dependent on the amount of incident light, but even in the absence of any light a small *dark current* is present [7]. In other words, dark current is image noise that should be removed from the measurements to increase the quality of images. This can be done by measuring a so-called *dark-frame* and subtracting it from the actual measurements. The dark-frame was measured by covering the front of the UHI-4 so that no light from outside entered the instrument. Dark current consists of two types of noise categories: temporal noise and fixed pattern noise [27]. While the first is a random disturbance that changes every time a capture is taken, the second has the same pattern in each frame for a specific sensor [27]. To account for the temporally varying component multiple *dark-frames* can be taken under the same condition and averaged to create a master frame. This improves the signal to noise ratio [28]. Hence, we used an average of multiple *dark-frames* in the following calibration and data analysis. Dark current is exposure time and temperature [29] dependent. Therefore, we measured the *dark-frame* for four different exposure settings and for three different (internal) temperatures.

In Fig. 6(a) we measured the dark current for 10, 100, 1000, and 10000 milli-seconds [ms], which represents the typical range of integration times, and calculated the mean of all spatial pixels for each wavelength over multiple frames. For 10 and 100 ms the dark current is more or less constant across the spectral range of the UHI-4 and the intensity is almost identical, ~50 digital counts. By increasing the exposure time to 1000 ms, the mean intensity across the spectrum increases by ~0.2%. However, distinct peaks emerge at 432 and 734 nm. These peaks are caused by so-called *hot pixels*, pixels that have a significantly higher intensity than neighboring pixels and thus influence the spectra of the averaged spatial component at certain wavelengths. By increasing the exposure time from 1000 to 10000 ms, the intensity across the spectrum increases by ~ 2.1% to ~51.5 digital counts, but at the wavelengths influenced by hot pixels, the intensity increases even more to ~53.5 digital counts. In addition, three more peaks appear at 466, 526, and 574 nm. The number of visible *hot pixels* increases with increased exposure time [30]. In total, we identified five hot pixels at 10000 ms and excluded them for the subsequent analysis.

In Fig. 6(b) we plotted the overall mean of all spectral and spatial pixels for internal temperatures of approximately −11°C, 30°C, and 49°C against the exposure time. The intensities for an exposure time up to 1000 ms are almost the same for −11°C and 30°C. The intensity for 10000 ms is slightly higher for 30°C than for −11°C. For an internal temperature of 49°C
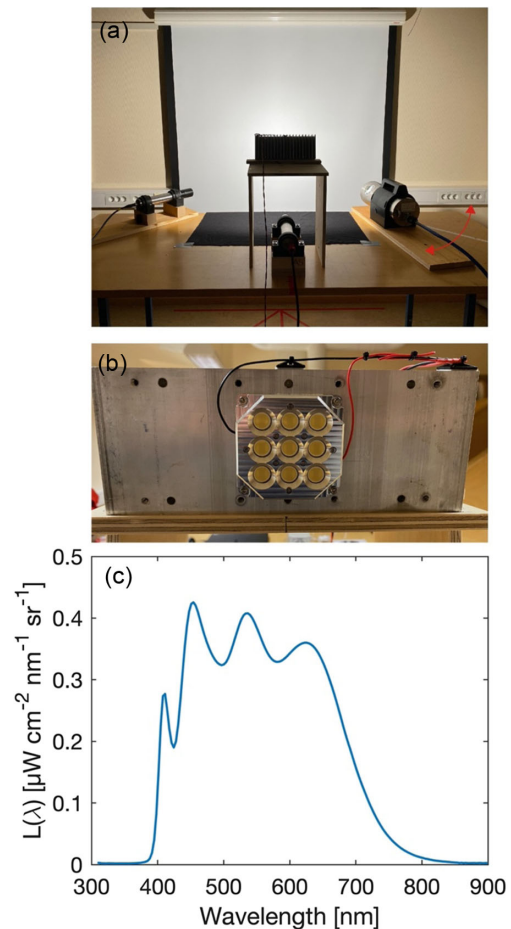
Fig. 5. (a) Setup for the radiometric calibration transfer. The UHI-4 and a RAMSES-ARC spectroradiometer are placed in a 45° angle pointing to the middle of a white projector screen. The UHI-4 can be rotated (red arrow) for ensuring that all parts of the FOV of the UHI-4 can be pointed to the middle of the target for ensuring identical light levels. The light source is centrally placed on a platform. (b) Self-made light source consisting of 3 × 3 LEDs on an aluminum cooling block. (c) $L(\lambda)$ spectrum of the light source measured with a RAMSES-ARC spectroradiometer.

the intensities are similar for 10 ms compared to the other internal temperatures but increase to 51.9 for 1000 ms and to 64.4 for 10000 ms. This is a significant increase in intensity, which shows that it is important to consider the operating temperature for the UHI-4, the medium it is deployed in, and the duration of deployment. If it is deployed for longer periods of time at room temperature or at higher temperatures in air it is recommended to subtract temperature and exposure dependent dark-frames from the measurements to ensure a result of good quality. However, an internal temperature of 49°C was only reached when measuring continuously over several days at room temperature. We plan to use the UHI-4 in waters with temperatures ranging from −2°C to ~10°C. In addition, water has a much higher specific heat capacity than air and thus is more efficient in cooling. Results from an in-water field deployment in the Norwegian Sea in mid-June showed that the internal temperature was below 19°C. For field data we therefore suggest using the *dark-frame* derived from measurements at 30°C. We took three frames per exposure time (10, 100, 1000, and 10000
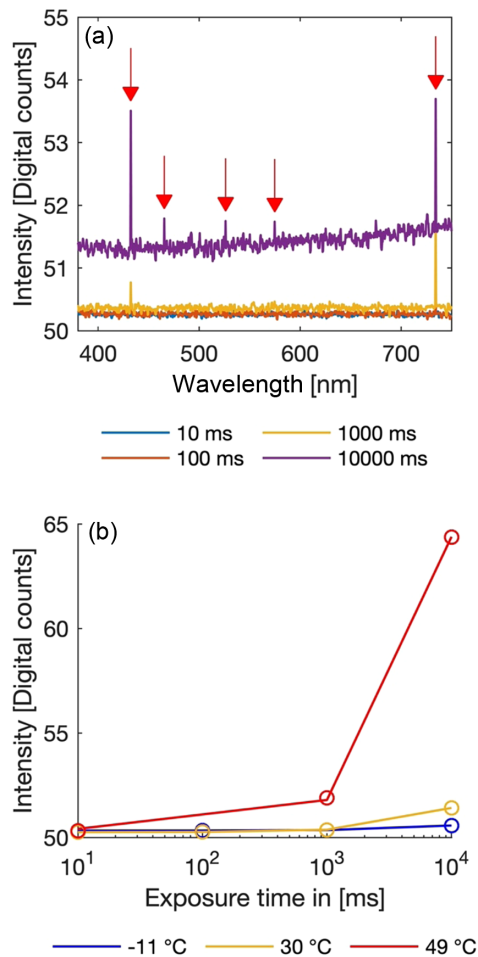
Fig. 6. (a) Dark current averaged over all spatial pixels plotted for each wavelength for different exposure settings at an internal temperature of ca. 30°C. Red arrows mark the influence of "hot pixels" on the averaged spectrum. Hot pixels were identified and excluded from subsequent analysis. (b) Overall mean dark current of all spatial and spectral pixels vs. exposure time for different internal temperatures. *Hot pixels* are excluded.

[ms]), merged them into one data-cube and calculated the mean frame. This *dark-frame* was used for calibration purposes and field measurements.
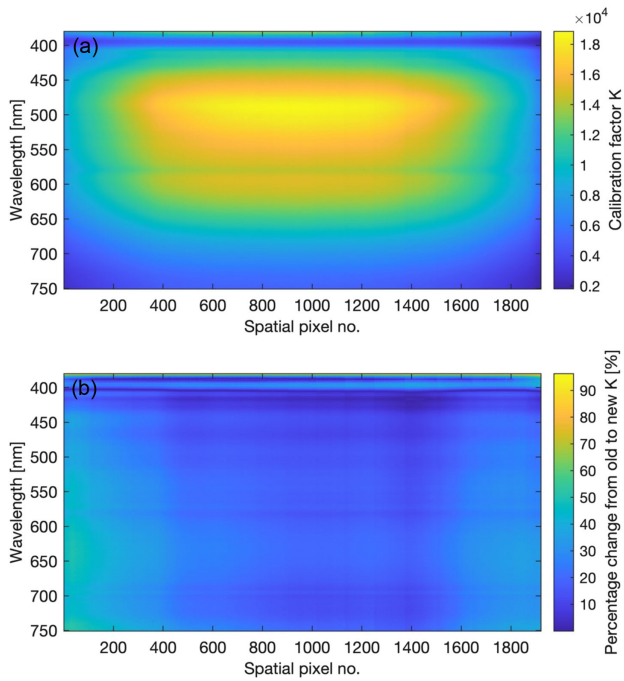
D. Radiometric Calibration Transfer

Radiometric calibration transfer of the UHI-4 allows us to convert digital counts into $L(\lambda)$ measured in the physical unit $[\mu W\ cm^{-2}\ nm^{-1}\ sr^{-1}]$. The previously described dark current measurements, and spectral and geometric calibrations, are necessary prerequisites to facilitate cross calibration against the NIST-traceable RAMSES-ARC spectroradiometer. The UHI-4 has a relatively large FOV. At the same time, it is important for the quality of the radiometric calibration that all pixels experience the same light intensities. Ideally, this would be done using a large integrating sphere to provide a uniform light field. Unfortunately, we do not have access to such a setup, as is the case for many laboratories who might still be interested in performing this type of calibration. We therefore decided to test a simpler and more affordable setup that could be more

readily replicated in other laboratory settings. Apart from the UHI-4 and the reference RAMSES-ARC spectroradiometer it consisted of a steady table, a projector screen, and a lamp. These things are usually available in most institutions and this setup can therefore be an example of how to carry out a low-cost radiometric calibration transfer.

Figure 5(a) shows the UHI-4 radiometric calibration transfer setup. The UHI-4 is placed on the right side and the reference sensor, a RAMSES-ARC spectroradiometer is placed on the left side. Both instruments, the UHI-4 and the RAMSES-ARC spectroradiometer, are pointing at a 45° angle to the projector screen to ensure that both instruments measure the same target area. The shortest/most direct distance between the instruments and the projector screen is 50 cm. The distance from the instruments to the measuring/target point is approximately 71 cm. In addition, a RAMSES-ACC-VIS radiometer measuring $E(\lambda)$ was aligned normally to the projector screen to monitor temporal fluctuations in the output of the lamp. We used the same custom made light source as in the geometric calibration. See Fig. 5(b) for the light source and Fig. 5(c) for its spectrum. The light source was positioned at a distance of 93 cm to the projector screen, pointing at ~13.5° below horizontal to center on the viewing plane of the UHI-4 and RAMSES radiometers. Mounting the lamp on a podium 39 cm above the table and placing black felt on the horizontal surface minimizes light reflections.

The large FOV of the UHI-4 instrument (~70° in air) is very difficult to fully illuminate with a uniform light field. Instead, it was decided to rotate the UHI-4 in 5° steps so that it is possible to fully illuminate the sensor by stages. For each measurement, a section of the sensor is pointing approximately at the center area of the projector screen. In this way, over the course of the measurements all parts of the sensor experience the same light level with only the portion pointing towards the center of the screen being selected for each 5° step and compiled in one matrix. To rotate the UHI-4 in a controlled manner it was placed on a wooden plank that was fixed with a screw on the table. The screw served as rotation point and was placed in a line with the center point of the front of the UHI-4. The 5° rotation steps were marked on the table and are illustrated by a red arrow in Fig. 5(a).

By performing simultaneous measurements of the RAMSES-ARC spectroradiometer and the UHI-4 for each rotation step it was possible to merge the 5° measurements into a matrix for the UHI-4 that have experienced the same light intensities. At the same time the RAMSES-ARC measurements were also merged into a reference matrix. Inserting these two matrices together with the *dark-frame* and the exposure time in Eq. (6) calculates a calibration factor K for each spectral and spatial pixel [Fig. 7(a)]. This matrix can be used to convert UHI-4 raw data to $L(\lambda)$ measured in the physical unit $[\mu W\ cm^{-2}\ nm^{-1}\ sr^{-1}]$. To compare the "new" calibration with the manufacturer's calibration from 2017 we calculated the percentage difference of the calibration factors K [Fig. 7(b)]. The result shows that the percentage difference is most distinctive for the wavelengths between 380 and ~410 nm. While it is below 30% for the majority of the matrix, for wavelengths close to the lower limit of the wavelength range at ~380 nm, the difference reaches as much as 90%. However, this difference should be interpreted

Fig. 7. (a) Radiometric calibration factors of UHI-4. (b) Percentage difference between own calibration to manufacturer's calibration from 2017. The difference is most distinctive for the wavelengths between 380 and ca. 410 nm.

with caution, since both calibration lamps provide very little light in this wavelength range. There is also a noteworthy difference of ~50% for the outermost spatial pixels on the left side and ~40% on the right side. A possible reason for this may be the different setup for the radiometric calibration. While the manufacturer placed the UHI-4 directly on the calibration lamp, the "new" calibration is done by rotating the instrument to ensure that all pixels experience the same amount of light:

$$K = \frac{\text{UHI}_{\text{raw}} - \text{darkFrame}}{\text{UHI}_{\text{exposuretime}} \cdot \text{Trios}_{\text{calibrated}}}. \tag{6}$$

E. Field Demonstration in Air

To test the performance of the calibration we made comparative measurements of the UHI-4 and the RAMSES-ARC spectroradiometer in air. Both instruments were mounted on a terrace on top of a university building (Tromsø, Norway) to minimize shading effects (Fig. 8). Since the UHI-4 has a much larger FOV (~70°) than the RAMSES-ARC spectroradiometer (~7°) we used two different setups. For the comparison of the UHI-4 center pixels we mounted both instruments on a wooden platform pointing straight up towards the sky at 0° angle from zenith [Fig. 8(a)]. For the comparison of the outermost UHI-4 pixels we used the same setup but inclined the RAMSES-ARC spectroradiometer at an angle of 31° from zenith [Fig. 8(b)]. To ensure the greatest possible comparability of both instruments we calculated the mean for the UHI-4 spatial pixels in an ~7° FOV so that the data presented from both instruments have approximately the same FOV.

The measurements for the 0° setup were carried out between 13:00 and 19:00 on 16.02.2022, with an ~15-min interval between measurements. See Fig. 8(c) for the measured spectra in the time interval 13:00 to 16:45. From 17:00 onwards the sensitivity of the RAMSES-ARC spectroradiometer was insufficient for a comparison across the whole spectrum and was therefore disregarded. The measurements for the 31° setup were carried out between 14:30 and 20:30 on 16.02.2022, again using an ~15-min interval between observations. Timestamps for both setups were manually synchronized across both instruments. Input from [18] was used for extracting the timestamps and checking the synchronization result in MATLAB scripts. See Fig. 8(d) for the measured spectra of both instruments for the 31° setup. Calibrated spectra of the UHI-4 and the RAMSES-ARC spectroradiometer match well in both shape and intensity for wavelengths from ~410 to 750 nm. The UHI-4 loses sensitivity below 400 nm and there is a dip between 400 and 410 nm that appears to be a systematic feature that is currently unresolved. This analysis suggests that the radiometric calibration (transfer) of the UHI-4 instrument is probably only valid for wavelengths from 410 to 750 nm.

To examine the difference between the two instruments more closely we calculated the relative error/deviation between the UHI-4 and the RAMSES-ARC spectroradiometer and plotted them in Fig. 8(e) for the 0° setup and in Fig. 8(f) for the 31° setup. The mean deviation across the spectrum is 7.6% for the 0° setup and 8.4% for the 31° setup. The median deviation is 3.7% for the 0° setup and 3.1% for the 31° setup. The results clearly illustrate the large deviations below 400 nm and the smaller, but still significant, deviation between 400 and 410 nm. From 414 nm onwards the deviation is relatively constant, but slowly increases with longer wavelengths.

Based on these plots we selected the wavelength range from 414 to 750 nm to examine the linearity. We plotted the $L(\lambda)$ of the UHI-4 against the $L(\lambda)$ of the RAMSES-ARC spectroradiometer for both setups in Figs. 8(g) and 8(h). The axes are on a log scale because the data spans several decades. Colors represent wavelengths in this figure. To assess the linearity, we used the linear least squares method in MATLAB for fitting a line. This method uses the mean value of the data for calculating a best fit line. However, the mean value will be heavily skewed towards large values, while the small values from measurements close to the sensitivity threshold would be effectively weighted close to zero [32]. Since the data spans over several decades and we would like to assess the linearity across the whole range we log-transformed both the RAMSES-ARC spectroradiometer and the UHI-4 data before we fitted the line [32]. The resulting line coefficients with 95% interval in brackets were $p_1 = 1.0054 \, (1.0042, 1.0066)$ and $p_2 = 0.0107 \, (0.0093, 0.0120)$ for the 0° setup and $p_1 = 0.9988 \, (0.9971, 1.0004)$ and $p_2 = -0.0056 \, (-0.0072, -0.0041)$ for the 31° setup. The coefficient p_1 is the slope of the line and is for both linear models very close to one, which indicates together with the plot a direct proportional linear relationship and a high correlation between the two sensors. The coefficient p_2 is the intercept and for both linear models close to zero, which fits with the expectation for a genuine linear relationship. The R-square value, a measure of
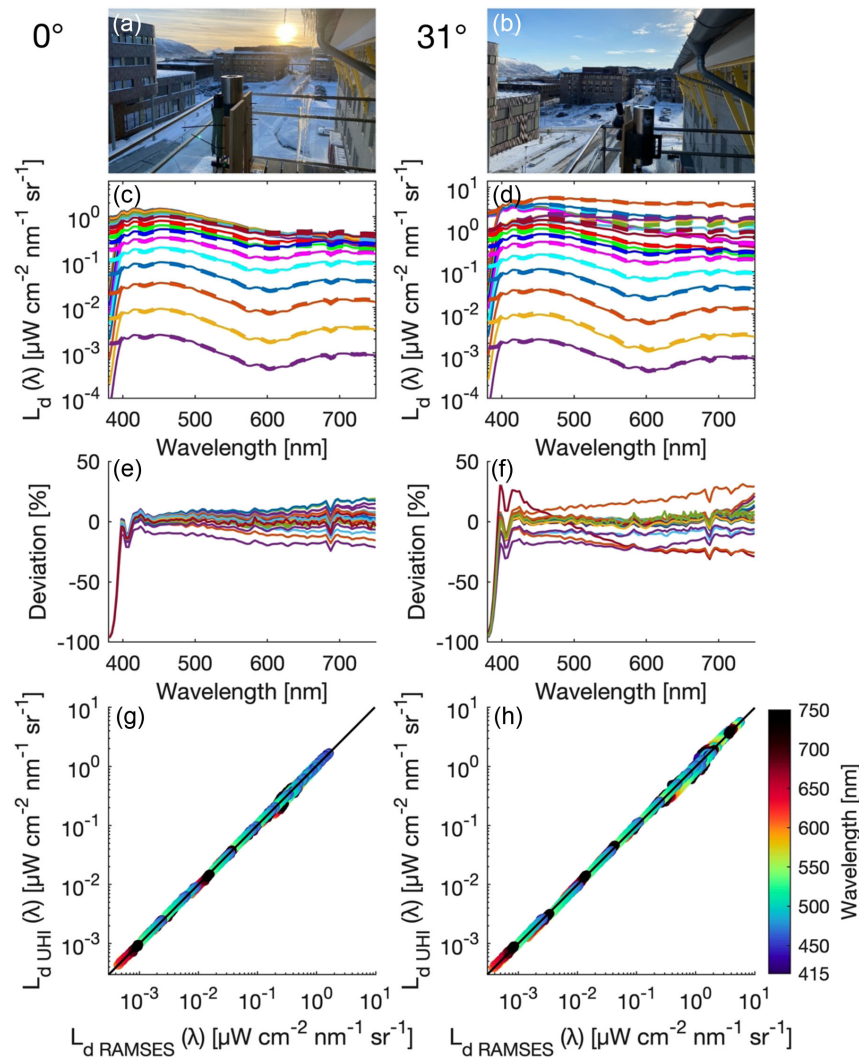
Fig. 8. (a), (b) Setup for comparing the UHI-4 with a RAMSES-ARC spectroradiometer. Both instruments are mounted on wooden frames next to each other. For comparing the UHI-4 center pixels both instruments are pointing directly up (0°), while for comparing the UHI-4 outermost 7° pixels the RAMSES-ARC spectroradiometer was placed in a 31° inclination so that the FOV fits with the 7° FOV of the TriOS sensor. (c) Downwards spectral radiance $L_d(\lambda)$ spectra measured by the UHI-4 (continuous line) and the RAMSES-ARC spectroradiometer (dashed line) 0° setup in an ~15-min interval from 13:00 to 16:45 on 16.02.2022. (d) $L_d(\lambda)$ spectra measured by the UHI-4 (continuous line) and the RAMSES-ARC spectroradiometer (dashed line) 31° setup in an ~15-min interval from 14:30 to 20:30 on 28.03.2022. (e), (f) Deviation between UHI-4 and RAMSES-ARC measurements in percent. There is a strong deviation for the wavelengths from 380 to 400 nm and an abrupt change in the 400–411 nm region. From 414 nm onwards the deviation is relatively constant, but slowly increasing with longer wavelengths. Hence, the wavelength range from 414 to 750 nm can be used for looking at the linearity. The deviations are larger for the 0° setup than for the 31° setup. (g), (h) The calibrated measurements for both sensors are plotted against each other on log scale. Colors represent wavelengths (colors created with MATLAB function from [31]). The black lines represent the best fit lines in log-space, which show a good linear behavior for both setups.

how well the regression model fits the observed data, is 0.9990 for the 0° setup and 0.9981 for the 31° setup. This means that 99.9% of variance of the dependent variable (UHI-4 instrument) is explained by the independent variable (RAMSES-ARC spectroradiometer) for the 0° orientation and 99.81% for the 31° orientation. At the same time the SSE value, which measures the total deviation of the response values from the fit to the response values [33], is 1.892 for the 0° orientation and 4.112 for the 31° orientation. The RMSE value, the standard deviation of the residuals, is 0.0256 for the 0° orientation and 0.0392 for the 31° orientation. Based on the goodness of fit values, we

conclude that the linear models fit the data well and are useful for prediction. This confirms that the calibration performs well under field conditions in air and can be used to measure $L(\lambda)$ in absolute units.

F. Field Demonstration in Water

To assess the performance of the calibration (transfer) in water we mounted the UHI-4 on a profiling frame designed for measuring *in situ* data for verification of remote sensing data. The

UHI-4 was pointing downwards measuring upwelling radiance, $L_u(\lambda)$. A RAMSES-ARC spectroradiometer pointing downwards was used as a reference. In addition, we mounted a RAMSES-ACC sensor pointing upwards for measuring downwards planar irradiance $E_d(\lambda)$. A round weight mounted below the UHI-4 ensured that the radiometric frame and its instruments were as stable as possible and influenced as little as possible by currents or ship movement during deployment. See Fig. 9(a) for a picture of the radiometric frame and Fig. 9(b) for a picture of the deployment using a crane on the research vessel R/V Helmer Hanssen. The field demonstration was carried out on a research cruise in the Norwegian Sea from 07.–14.06.2022 as part of the SFI Harvest project ([34]). We sampled nine radiometric stations.

Figure 9(c) shows the $L(\lambda)$ profiles at different depths for the UHI-4 and the RAMES ARC spectroradiometer for Station 08 (date: 11.06.2022, latitude 69°43.63, longitude 10°01.81, wind 9.4 m/s, sea condition: 1.5 m swell, total cloud cover,

depth 2911 m). We applied the radiometric calibration determined above to the UHI-4 data and interpolated them to the RAMSES-ARC wavelengths for better comparability. In addition, we applied theoretical immersion factors for a radiometer window of fused silica and a salinity of 35 psu from Table 4 in [35]. This approach is supported by [21] who showed that the averaged absolute relative difference between a measured and a theoretical immersion factor is relatively small (∼2%) for a similar UHI-4 model and the averaged difference in immersion factor between the center and the outermost pixel is only 1% to ∼3% across its half angle FOV [21]. Since the immersion factor in [35] was only defined at certain wavelengths from 400 to 700 nm we interpolated and extrapolated the immersion factor to the RAMSES-ARC wavelengths. When we compare the magnitude and spectral distribution of data for both sensors, we see that they match well in the wavelength range from ca. 410 to 550 nm. As before, the UHI-4 struggles for sensitivity below 410 nm, consistent with the field demonstration in air. For depth greater than 2 m, the RAMSES-ARC spectroradiometer
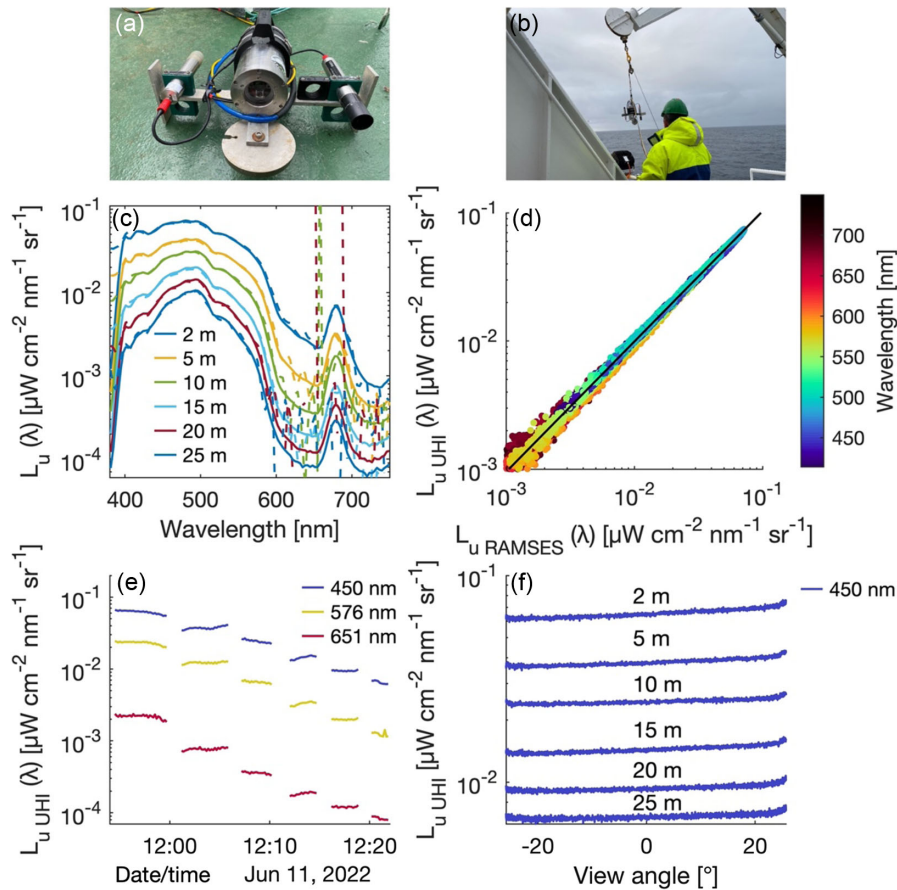
Fig. 9. (a) Profiling radiometric frame with UHI-4 mounted in the middle, pointing down, measuring upwards spectral radiance $L_{u\,\text{UHI}}(\lambda)$. A RAMSES-ARC spectroradiometer measuring upwelling $L_{u\,\text{RAMSES}}(\lambda)$ for comparison is mounted on the right side approximately at the same height. A RAMSES-ACC-VIS radiometer is mounted on the left side for measuring $E_d(\lambda)$. (b) Deployment of the radiometric frame with a crane from the research vessel R/V Helmer Hanssen. (c) $L_u(\lambda)$ spectra measured with the UHI-4 (continuous line) and RAMSES-ARC spectroradiometer (dashed line) on 11.06.2022 in the Norwegian Sea at Radiometric Station 08 of the "SFI Harvest" cruise. The two instruments show good agreement if there is enough light for the RAMSES-ARC spectroradiometer. From depth 5 m and below the RAMSES-ARC spectroradiometer reaches its sensitivity level for the wavelength range from 600 to 750 nm. This is expected as red light is absorbed quickly in water and therefore less light is available in this wavelengths range. (d) $L_{u\,\text{UHI}}(\lambda)$ measurements plotted against $L_{u\,\text{RAMSES}}(\lambda)$ measurements. Colors represent wavelengths (colors created with MATLAB function from [31]). The black line is the best fit line in log-space. It shows a close to linear relationship between the two sensors. (e) $L_{u\,\text{UHI}}(\lambda)$ profiles for three selected wavelengths. (f) Angular distribution of $L_{u\,\text{UHI}}(\lambda)$ at 450 nm for different depths.

becomes significantly noisier than the UHI-4 for wavelengths between 550 and 750 nm. This is due to the effect of water absorption rapidly attenuating light levels in the red and near infrared, the limit of only having a single integration time for recording the entire spectrum, which is set by the maximum recorded signal (in the green in this case), limited dynamic range for the RAMSES-ARC detector, and a lower signal to noise ratio in the RAMSES-ARC spectroradiometer compared to the UHI-4. Hence, we disregarded this data when we plotted the UHI-4 against the RAMES-ARC spectroradiometer in Fig. 9(d). The spectra in Fig. 9(c) can be used as a proxy for *in vivo* absorption spectra for phytoplankton. The peak in the red part of the spectrum at ∼678 nm indicates that most chlorophyll a is bonded to photosystem I (outlined in [36]). This indicates that diatoms, dinoflagellates, and prymnesiophytes are less likely to be the dominant group but may be indicative of small prasinophytes. The absorption in the green part of the spectrum should be low at wavelengths longer than 535 nm (fucoxanthin and peridinin containing pigment groups). This also indicates that cells present are not diatoms, dinoflagellates, or prymnesiophytes. However, further in-depth analyses together with species ground truthing data are necessary for confirming this.

To assess the linearity, we fitted a line in MATLAB using the linear least squares method on log-transformed RAMSES-ARC and UHI-4 data [Fig. 9(d)]. The polynomial coefficients with 95% interval in brackets are $p_1 = 1.0174$ (1.0162, 1.0186) and $p_2 = 0.0302$ (0.0278, 0.0326). The goodness of fit values are an R-square of 0.9969, a SSE of 6.9233, and a RMSE value of 0.0284 and confirm that the model is useful for prediction. Figure 9(d) verifies visually that there is a linear relationship between the observations of the two sensors. It can therefore be concluded that the calibration (transfer) performs well in water and can be used for measuring $L(\lambda)$ in absolute units underwater. Colors in the plot represent wavelengths. Figure 9(e) shows the $L_{u\,\text{UHI}}(\lambda)$ profiles for three selected wavelengths at 450 nm (blue), 576 nm (yellow), and 651 nm (red) against time. The step-wise decrease in $L_{u\,\text{UHI}}(\lambda)$ can be explained in that the radiometric frame was lowered step-by-step. Red light is absorbed fastest by seawater, while blue light is absorbed least and therefore penetrates furthest in these waters.

Part of the novelty of the UHI-4 is that it can measure the angular distribution of $L(\lambda)$. We therefore plotted the $L_{u\,\text{UHI}}(\lambda)$ for each spatial pixel, represented by the view angle, at a wavelength of 450 nm for specific depths in Fig. 9(f). The $L_{u\,\text{UHI}}(\lambda)$ distribution is relatively flat across the spatial axis, reflecting the fact that the upwards $L(\lambda)$ is generated in the ocean by diffuse reflectance and that the FOV is restricted to ∼ ± 25°. Potentially, more variation would be visible with an even larger FOV. There is a slightly skewed aspect to the spatial distribution, which could be a residual artifact from the calibration process or could potentially be a consequence of uncorrected tilt when deploying the sensors in water.

4. CONCLUSIONS

We have developed a relatively low-cost calibration transfer approach that allows us to investigate spectral, geometric, and radiometric performance of a commercial push broom hyperspectral imaging instrument (UHI-4, Ecotone AS, Norway)

with a relatively wide field of view. Comparison with previous manufacturer's calibration suggest that our approach is at least useful for monitoring for significant deviations in the performance of an instrument and may be sufficiently robust to allow primary cross-calibration if circumstances require it. Our hope is that this might enable users to conduct their own calibration transfer and verify the manufacturer's calibration.

Calibrations performed using our approach were broadly consistent with those of the manufacturer performed some years previously. Differences between calibrations could reflect real changes in instrument performance over that period associated with wear and tear through usage. Alternatively, the residual difference may reflect small differences in the calibration approaches used.

Our calibration work has established that the UHI-4 instrument is generally performing to specifications in most key areas, but that the radiometric calibration transfer is probably only valid from 410 to 750 nm. The dark current measurements indicate that under normal operating conditions a constant *dark-frame* can be used for internal temperatures up to 30° and independent of exposure time, which greatly simplifies deployment processes and data processing. Field demonstrations in air and in water demonstrate excellent co-linearity with a RAMSES-ARC spectroradiometer over several orders of magnitude. The UHI-4 instrument appears to offer greater dynamic range for a given integration time, as evidenced by the lower noise levels in the red and near infrared for in-water data collected below 2 m depth at our sample station. The wide field of view of the UHI-4 has been geometrically calibrated permitting observation of $L(\lambda)$ signals over a linear swath of angles covering approximately ±35° in air and ±25° in water. Together with radiometric calibration transfer, this permits measurement of elements of the hyperspectral $L(\lambda)$ distribution that would otherwise be very difficult to measure with a single sensor. Initial tests as an upwards radiance sensor broadly confirm radiometric performance across the field of view but are less impressive in terms of revealing capacity to provide interesting spatial information as the upwards $L_u(\lambda)$ field is relatively featureless. The true merit of this instrumental approach will be demonstrated in future deployments where the angular structure of the light field is more varied and scientifically relevant. We expect these experiments to involve deployments on autonomous underwater vehicles where push broom imaging will allow measurement of $L(\lambda)$ distributions under sea-ice [21], wave focusing effects, and distributions of artificial light around ships and other installations. The high spectral resolution of the UHI-4 offers a lot of potential information about phytoplankton pigments (bio-optical taxonomy) and gives scope to better resolve features that are probably there in the RAMSES-ARC data, but harder to extract. Furthermore, it offers potential to ground truth hyperspectral data from hyperspectral CubeSats, e.g., HYPSO [37], and could fill in remaining gaps for, e.g., PACE [38].

REFERENCES

1. National Aeronautics and Space Administration (NASA) Science Mission Directorate, "Anatomy of an electromagnetic wave," 2010, retrieved 18.04.2024, 2024, http://science.nasa.gov/ems/02_anatomy.
2. P. G. Falkowski and J. A. Raven, *Aquatic Photosynthesis* (Princeton University, 2013).
3. K. Tessmar-Raible, F. Raible, and E. Arboleda, "Another place, another timer: marine species and the rhythms of life," Bioessays **33**, 165–172 (2011).
4. S. H. Haddock, M. A. Moline, and J. F. Case, "Bioluminescence in the sea," Annu. Rev. Mar. Sci. **2**, 443–493 (2010).
5. G. C. Hays, "A review of the adaptive significance and ecosystem consequences of zooplankton diel vertical migrations," in *Migrations and Dispersal of Marine Organisms* (2003), Vol. **503**, pp. 163–170.
6. J. H. Cohen, J. Berge, M. A. Moline, *et al.*, "Light in the polar night," in *POLAR NIGHT Marine Ecology: Life and Light in the Dead of Night*, J. Berge, G. Johnsen, and J. H. Cohen, eds. (Springer International Publishing, 2020), pp. 37–66.
7. C. D. Mobley, *Light and Water: Radiative Transfer in Natural Waters* (Academic, 1994).
8. J. L. Mueller, A. Morel, R. Frouin, *et al.*, *Ocean Optics Protocols For Satellite Ocean Color Sensor Validation, Revision 4. Volume III: Radiometric Measurements and Data Analysis Protocols* (2003).
9. C. D. Mobley and K. Voss, "OCEAN OPTICS Web Book- geometrical radiometry," 2021, retrieved 19.04.2024, 2024, https://oceanopticsbook.info/view/light-and-radiometry/geometrical-radiometry.
10. C. Katlein, M. Schiller, H. J. Belter, *et al.*, "A new remotely operated sensor platform for interdisciplinary observations under sea ice," Front. Mar. Sci. **4**, 281 (2017).
11. V. Vabson, J. Kuusk, I. Ansko, *et al.*, "Field intercomparison of radiometers used for satellite validation in the 400–900 nm range," Remote Sens. **11**, 1129 (2019).
12. J. T. Kirk, *Light and Photosynthesis in Aquatic Ecosystems* (Cambridge University, 1994).
13. H. P. Stahl, "Rules for optical metrology," in *22nd General Congress of the International Commission for Optics (ICO)* (2011).
14. G. Johnsen, A. Zolich, S. Grant, *et al.*, "All-sky camera system providing high temporal resolution annual timeseries of irradiance in the Arctic," Appl. Opt. **60**, 6456–6468 (2021).
15. Ecotone AS, *Ecotone UHI4 User Manual* (2017).
16. Hamamatsu Photonics K.K., "ORCA®-spark Digital CMOS camera C11440-36U," 2024, retrieved 29.01.2024, https://www.hamamatsu.com/content/dam/hamamatsu-photonics/sites/documents/99_SALES_LIBRARY/sys/SCAS0114E_C11440-36U.pdf.
17. Z. Volent, G. Johnsen, and F. Sigernes, "Kelp forest mapping by use of airborne hyperspectral imager," J. Appl. Remote Sens. **1**, 011503 (2007).
18. OpenAI, *ChatUiT (Model: ChatGPT-3.5)* (2024).
19. J. Støren, Ecotone AS (personal communication, 2024).
20. TriOS Mess- und Datentechnik GmbH, *Brochure RAMSES* (2024).
21. H. Liu, N. Summers, Y.-C. Chen, *et al.*, "Pixelwise immersion factor calibration for underwater hyperspectral imaging instruments," Opt. Express **32**, 19854–19880 (2024).
22. Newport Corporation, "Spectral calibration lamp, Argon, 10 mA, 500 hour rated life," 2024, retrieved 23.01.2024, https://www.newport.com/p/6030.
23. Newport Corporation, "Spectral calibration lamp, Hg (Ar), 18±5 mA, 5000 hour rated life," 2024, retrieved 23.01.2024, https://www.newport.com/p/6035.
24. Oriel® Instruments, "Typical spectra of ORIEL INSTRUMENTS spectral calibration lamps," (Newport Corporation).
25. SPECIM Spectral Imaging Ltd. (personal communication, 2024).
26. R. Millard and G. Seaver, "An index of refraction algorithm for seawater over temperature, pressure, salinity, density, and wavelength," Deep Sea Res. A **37**, 1909–1926 (1990).
27. J. Sølhusvik, "INF5350–CMOS image sensor design, Lecture 5– Noise and modelling S/N," (University of Oslo, Department of Informatics, 2020).
28. R. Widenhorn, J. C. Dunlap, and E. Bodegom, "Exposure time dependence of dark current in CCD imagers," IEEE Trans. Electron Devices **57**, 581–587 (2010).
29. R. McGrath, J. Doty, G. Lupino, *et al.*, "Counting of deep-level traps using a charge-coupled device," IEEE Trans. Electron Devices **34**, 2555–2557 (1987).
30. G. H. Chapman, R. Thomas, R. Thomas, *et al.*, "Increases in hot pixel development rates for small digital pixel sizes," Electron. Imaging **28**, 1–6 (2016).
31. S. Eddins, "Color tools for MATLAB," GitHub, 2024, https://github.com/mathworks/matlab-color-tools/releases/tag/v2.1.2.
32. B. Schartmüller, P. Anderson, D. McKee, *et al.*, "Development and calibration of a high dynamic range and autonomous ocean-light instrument to measure sub-surface profiles in ice-covered waters," Appl. Opt. **62**, 8308–8315 (2023).
33. A. Coster, 2024, retrieved 19.01.2024, https://web.maths.unsw.edu.au/~adelle/Garvan/Assays/GoodnessOfFit.html.
34. https://www.sfiharvest.no.
35. G. Zibordi, "Immersion factor of in-water radiance sensors: assessment for a class of radiometers," J. Atmos. Ocean. Technol. **23**, 302–313 (2006).
36. G. Johnsen and E. Sakshaug, "Biooptical characteristics of PSII and PSI in 33 species (13 pigment groups) of marine phytoplankton, and the relevance for pulse-amplitude-modulated and fast-repetition-rate fluorometry 1," J. Phycol. **43**, 1236–1251 (2007).
37. S. Bakken, M. B. Henriksen, R. Birkeland, *et al.*, "Hypso-1 CubeSat: first images and in-orbit characterization," Remote Sens. **15**, 755 (2023).
38. G. Meister, J. J. Knuble, U. Gliese, *et al.*, "The ocean color instrument (OCI) on the plankton, aerosol, cloud, ocean ecosystem (PACE) mission: system design and prelaunch radiometric performance," IEEE Trans. Geosci. Remote Sens. **62**, 5517418 (2024).